Plasma Sources Science and Technology

PAPER • OPEN ACCESS

Inductive probe measurements in a rotating magnetic field thruster

To cite this article: Christopher L Sercel *et al* 2023 *Plasma Sources Sci. Technol.* **32** 105017

OPEN ACCESS
IOP Publishing
Plasma Sources Science and Technology
Plasma Sources Sci. Technol. **32** (2023) 105017 (14pp)
https://doi.org/10.1088/1361-6595/acfd5a

Inductive probe measurements in a rotating magnetic field thruster

Christopher L Sercel*, **Tate M Gill** and **Benjamin A Jorns**

University of Michigan, Ann Arbor, MI, United States of America

E-mail: csercel@umich.edu

Received 20 March 2023, revised 11 August 2023
Accepted for publication 26 September 2023
Published 30 October 2023

Abstract

The induced magnetic field during acceleration in a pulsed rotating magnetic field (RMF) thruster is experimentally investigated. A two-axis Bdot probe is employed to characterize the time-resolved evolution of the fields in a 5 kW-class test article. This device is operated at an average power of 4 kW with an RMF frequency of 415 kHz, pulse widths of 125 μs, and a repetition rate of 155 Hz. Plasma currents induced in the thruster are shown to reach 2500 A and to have sufficient magnitude to form a field-reversed configuration plasmoid. The Lorentz force resulting from the induced magnetic field contributes $\sim$25% of measured thrust at this operating condition. Of this Lorentz thrust, $\sim$58% is due to plasma current interaction with the steady applied bias field, while the remainder is caused by interaction with secondary induced currents in nearby structural elements. This structure force is predicted to scale quadratically with plasma current magnitude. These results are discussed in the context of the historically low performance of these devices and strategies for improving their operation are presented.

Keywords: inductive probing, electric propulsion, pulsed plasmas, rotating magnetic field, field-reversed configuration, RMF, FRC

1. Introduction

The rotating magnetic field (RMF) thruster, a member of a family of devices known as inductive pulsed plasma thrusters (IPPTs), employs a RMF to induce directed azimuthal current in a seed plasma along with enhanced ionization of the seed plasma. This current interacts with the radial component of any magnetic fields present to produce an axial body force on the plasma, causing plasma ejection and thus generating impulse. The RMF thruster shares many of its potential strengths with other in-family devices such as the pulsed inductive thruster (PIT) [1], the conical theta-pinch thruster [2], and the Faraday accelerator with radio-frequency assisted discharge (FARAD) thruster [3]. These include high throttlability while maintaining efficiency and specific impulse, high specific power [4], and *in-situ* resource utilization (ISRU) compatibility. The RMF current drive scheme has the additional benefit that the induced plasma current depends on the RMF's rotational frequency rather than its magnitude [5], which is not the case for other more canonical IPPTs [6]. The RMF thruster can thereby avoid the prohibitively large current and voltage transients required for other IPPTs to operate. These transients pose a challenge for power supply design and switching circuit longevity.

Due to these potential advantages, multiple research groups have investigated this device. First among these studies was the work by MSNW, LLC and the University of Washington with their electrodeless Lorentz force (ELF) thruster. This RMF-based thruster was operated with nitrogen, air, oxygen, and xenon propellants in burst operation, i.e. with a limited number of consecutive pulses. Each pulse delivered between 10 and 70 Joules with an RMF frequency of 300 kHz. [7]. Because the burst operation precluded standard thrust stand measurement and the thruster itself was integrated mechanically with the vacuum chamber, performance could only be measured indirectly with a calibrated ballistic pendulum. The resulting per-shot impulse was used to infer thrust efficiency

* Author to whom any correspondence should be addressed.

of up to ∼8% [8] although this number does not include mass utilization, divergence effects, or losses associated with coupling power to the plasma. This group also performed path-finding demonstrations to show the thruster was capable of ISRU capability by testing with exotic propellants [9]. More recently, the Furukawa group at the Tokyo University of Agriculture and Technology has developed a test unit and performed electrical and plasma-based measurements. In lieu of burst mode operation, Furukawa *et al* operated their device with continuous pulsing, thus enabling time-averaged measurements of performance. Indirect measurements with a ballistic pendulum yielded thrust peaking at ∼7 mN for 3 kW operation at 60 sccm argon propellant flow rate and an RMF frequency of 700 kHz [10, 11]. Based on these reported values, we can infer a total efficiency of ∼0.5%. Finally, we have recently taken performance measurements on a test unit which shares design heritage with the ELF thruster. We supplied ∼4 kW of power at an RMF frequency of ∼415 kHz with xenon propellant flow ranging between 15 and 60 sccm. At these conditions, we performed the first, to our knowledge, published direct performance measurements with a thrust stand on an RMF thruster. Overall efficiency peaked at ∼0.5% with a thrust of ∼8 mN [12]. The major implication of these exploratory studies has been that despite its apparent advantages, the RMF's performance is not competitive with more mature electric propulsion technologies.

These low performance results invite the question of why the performance is low. We seek to understand what the dominant loss mechanisms are and how they scale for RMF thrusters. To address this question, we performed in our previous studies internal plasma probing measurements on an RMF test article to characterize efficiency modes. These studies [12, 13] showed that up to 50% of input energy is successfully coupled into the plasma from the RMF. This indicated that the overall efficiency loss was likely dominated by inefficient acceleration, the conversion of the input energy into directed flow. Further investigation yielded the result that radiation losses and wall losses are responsible for the loss of nearly all energy input to the plasma [14]. This conclusion is consistent with previous scaling arguments proposed by Weber in the context of the ELF thruster [8]. The role of wall losses is not unique to RMF devices, and has been observed in a number of low temperature inductively coupled devices (e.g. [15, 16]). The relatively narrow aspect ratio of RMF devices in particular lends itself to this loss process.

An equally important question in addition to efficiency losses for these thrusters is the effectiveness of the RMF current drive. For example, the RMF may not penetrate the plasma as expected due to screening caused by a combination of collisionality and classical skin depth. To this point, Furukawa's group performed azimuthal plasma current measurements directly in an RMF thruster. They showed that azimuthal currents are indeed induced by the RMF but at ∼2.5% of the theoretically expected value [17]. In our recently developed test article, the RMF magnitudes are higher and frequencies are lower, and therefore we expect a more effective RMF current drive owing to increased field penetration into the plasma. Indeed, we find in previous work that overall thruster performance increased with RMF field strength [12]. In the ideal case, however, the currents induced by the RMF—and by extension thruster performance—should be independent of this parameter. In light of these previous findings, there remains an open question as to the degree to which we drive azimuthal currents in our system, and more generally, the extent to which RMF contributes to thrust generation through the Lorentz force. Due to the critical role of the current drive mechanism in the RMF thruster, the need is apparent for plasma current density measurement to assess whether current generation and plasma acceleration behave as understood.

The goal of this work is to perform spatially and temporally resolved magnetic field and current density measurements during pulsed operation of an RMF thruster and to correlate these with magnetically induced force on the plasma. We organize the paper in the following way. In section 2 we overview the operating principles of the RMF thruster as they are presently understood as well as our probing techniques. In section 3, we present the experimental setup. In section 4 we detail the analysis performed on the probe data to arrive at data for the magnetic field, current density, and Lorentz force before presenting these results in section 5. In section 6 we discuss the physical significance of the results, and finally in section 7 we summarize our work and major conclusions.

2. Theory

In this section, we discuss the purported mechanism of acceleration in the RMF thruster and introduce the scaling laws and theories for its performance. Figure 1 shows the geometry of a canonical RMF thruster. A seed plasma is introduced to a plasma-bounding dielectric cone, which is surrounded by electromagnets which form the applied magnetic bias field. Two sets of saddle coils, which we denote as the RMF antennas, are clocked 90° relative to each other such that each set produces a magnetic field orthogonal to the other. The RMF is then generated by applying sinusoidal currents into each antenna with a 90° phase lag. The basic process of pulsed operation is thus: after seed plasma fills the cone, the RMF induces an azimuthal current in the plasma. This current, along with electric fields produced by the RMF, promote further ionization of the plasma. The azimuthal current interacts with the magnetic fields resulting from the bias magnets as well as transient currents induced in structural elements of the thruster. These latter currents arise from the response to the rapid onset of the azimuthal plasma current. The resulting Lorentz force is directed inwards and axially, serving to eject the plasma to produce thrust with measured ejected plasma densities $n_e \geqslant 10^{19}\ 1\ \mathrm{m}^{-3}$. Mass utilization (the conversion of inflow neutral atoms to ions) has been measured to be as high as 100% [13]. This process is then repeated at a desired repetition rate.

2.1. RMF current drive

Each RMF antenna effectively consists of a Helmholtz pair oriented transverse to the cone's axis, (x or y in figure 1) such that a current flowed through a given antenna produces a uniform magnetic field in that direction. Injecting a sinusoidal

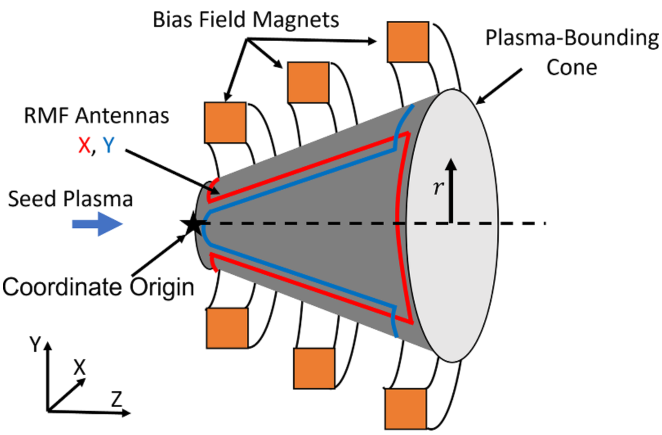

Figure 1. Schematic of geometry of the canonical RMF thruster illustrating coordinate convention and key elements.

current waveform though each antenna at a phase delay of 90° results in an approximately uniform RMF which can be described as

$$\vec{B}_{\mathrm{RMF}} = |B_{\mathrm{RMF}}| \left(\cos(\omega t)\,\hat{x} + \sin(\omega t)\,\hat{y}\right), \tag{1}$$

where $|B_{\mathrm{RMF}}|$ is the RMF magnitude and ω is the frequency of the applied sinusoidal current, referred to henceforth as the RMF frequency. It can be shown [5] under the assumptions of unmagnetized ions, magnetized electrons, isotropic plasma properties, and full field penetration into the plasma column, that the induced azimuthal current density is given by

$$j_\theta = \frac{-ne\omega r}{1 + 2\left(\frac{ne\eta}{|B_{\mathrm{RMF}}|}\right)^2}, \tag{2}$$

where n refers to the electron density, r is the radial coordinate as defined in figure 1, and η to the plasma resistivity. We note that we have used a scalar plasma resistivity because the current is driven primarily in only one direction. Physically, this equation shows that increasing the plasma density, RMF frequency, and field magnitude have the effect of leading to higher induced current density. This scaling provides a strong potential advantage over other pulsed inductive plasma devices because plasma currents can be induced without the need for high amplitude voltage or current transients in the driving circuit.

Per [18], equation (2) is valid provided there is complete RMF field penetration into the plasma:

$$\left(\frac{\nu_{\mathrm{ei}}}{\omega_{\mathrm{ce}}}\right)^2 \left(\frac{R}{\delta}\right)^2 << 1, \tag{3}$$

where $\omega_{\mathrm{ce}} = \frac{eB_{\mathrm{RMF}}}{m_e}$ is the RMF's electron cyclotron frequency, $\nu_{\mathrm{ei}} = \frac{\eta e^2 n_e}{m_e}$ is the electron-ion collision frequency, R is thruster radius, and $\delta = \sqrt{\frac{2\eta}{\omega\mu_0}}$ is the classical skin depth of the RMF. For our device, plasma densities have been measured to reach values above $n_e \approx 1\times10^{19}\ 1\,\mathrm{m}^{-3}$ with electron temperatures of $T_e \approx 9$ eV [14]. At our RMF angular frequency of $\omega = 2.6\times10^6$ rad s^{-2}, we measured an RMF field strength of approximately $B_{\mathrm{rmf}} = 5\times10^{-3}$ T. This corresponds to an electron cyclotron frequency of $\omega_{\mathrm{ce}} \approx 8.8$ GHz. With these plasma and RMF parameters, we find a classical skin depth of $\delta \approx 1$ cm and a Coulomb resistivity of $\eta \approx 1.75\times10^{-4}\,\Omega$-m. For these properties and with our thruster radius of $R = 10$ cm, the quantity on the left-hand side of equation (3) yields 2×10^{-4} such that the penetration condition is satisfied and equation (2) is valid. With these same plasma and RMF properties, we also find that $|B_{\mathrm{RMF}}|/\sqrt{2}ne\eta \approx 10$ such that equation (2) yields $j_\theta \approx -ne\omega r$. The expected RMF current density in our device is thus independent of RMF field strength and depends only the local plasma density and angular frequency of the RMF. These quantities also yield an expected value for j_θ on the order of 10 A cm^{-2}, which is consistent with our experimental measurements (section 5).

2.2. Thrust generation

Once the plasma current has been induced, it will interact via the Lorentz force with any magnetic fields present. Thruster performance depends on the axial component of this force:

$$F = \int_V B_r j_\theta \mathrm{d}^3 r, \tag{4}$$

where B_r refers to the radial component of the magnetic field, $\mathrm{d}^3 r$ is the differential volume element, and V denotes the volume of space wherever plasma exists. We identify three contributions to the magnetic field present in an RMF thruster:

$$\vec{B} = \vec{B}_0 + \vec{B}_{\mathrm{self}} + \vec{B}_{\mathrm{struct}}. \tag{5}$$

Here $\vec{B}_0$ denotes the field produced by the DC electromagnets, $\vec{B}_{\mathrm{self}}$ is the self-field produced by the azimuthal plasma current, and $\vec{B}_{\mathrm{struct}}$ is the structure field resulting from transient currents induced in conductive structural elements of the thruster by the rapid onset of the plasma current.

The expressions which describe how each of these magnetic field terms scale with the induced plasma current is derived in the appendix. We find that the bias field is independent of the plasma current, while the self-field and the structure field depend linearly on the plasma current. With this being said, we do not expect net axial contribution to impulse from the self-field because it physically represents the interaction of one section of the plasma with another. Since Newton's Second Law implies that no system can accelerate its own center of mass, we expect that the self-field should be able to cause expansion of the plasma but not net axial acceleration. With this in mind, we thus can motivate how plasma current generates thrust by writing equation (4) as

$$F = \alpha_0 I_\theta + \alpha_{\mathrm{struct}} I_\theta^2, \tag{6}$$

where I_θ refers to the total azimuthal plasma current, and α is a time-dependent geometric factor unique to each field which depends on how the plasma currents are distributed spatially. Physically, equation (6) shows that we expect the bias field force to increase linearly with the induced plasma currents while the structure field force increases quadratically.

As with other electromagnetic thrusters, the quadratic scaling with current indicates a potential advantage for pulsed operation, where high momentary currents can drive enhanced thrust. This is in contrast to an operating mode where lower steady current is maintained at the same average power.

In the latter sections of this work, we separate each magnetic field's contribution to the overall force with the goal of identifying whether the quadratically-scaling structure force term dominates for our test article. This is performed by first recognizing that since the bias field is constant, any time-varying fields are due to the self and structure fields. Next, we note that the self-field is caused by currents contained in the plasma, while the structure field is caused by currents outside the plasma. Therefore, by directly measuring the plasma currents, the self-field can be determined via the Law of Biot-Savart. The structure field is described by any discrepancy between the calculated self-field and the measured time-varying field.

3. Experimental setup

In this section, we detail the experimental setup used to obtain our results. We first describe the test article and briefly motivate its design. We then discuss our probe techniques used to acquire the data before describing the facility in which these tests were performed.

3.1. Test article

The unit under test, the PEPL RMFv2 Thruster pictured in figure 2(a), was designed to follow heritage from previous thrusters such as the ELF thruster [8]. An in-depth discussion of the design can be found in [12]. In brief, three electromagnets provide the bias field and double as flux-conserving surfaces—elements which serve to enhance the structure field. The RMF antennas are constructed from copper tubing, through which we flow water to maintain constant temperature, and therefore resistance, of the antennas. A plasma-bounding cone is constructed from a rolled mica sheet. The support structure of the device is made from G10 fiberglass laminate as it is non-conductive and therefore minimizes unintended mutual inductance effects. The plasma-bounding cone is approximately 33 cm long with an upstream diameter of 6 cm and a downstream diameter of 20 cm. A seed plasma is formed by flowing xenon through an upstream LaB_6 hollow cathode discharging to an annular anode. During operation, xenon gas is flowed from a downstream annular injector into the cone to increase neutral residence time. We note that the cathode consumed ≈400 W (≈10% of the total power) during this test, which would represent a major efficiency loss for a flight-like system. However, the intention of this study was to focus on the internal plasma physics of the RMF thruster. We chose to use a cathode due to the availability of equipment and institutional experience with this device. Other RMF thrusters (e.g. [8]) have used lower power electrodeless ionization schemes to good effect.

To produce the oscillating current, each antenna is paired with a tuning capacitor bank to form a series LC circuit with a resonant frequency of 415 kHz. As each tuning capacitor bank has capacitance 42 nF, the antennas are estimated to have an inductance of $L \approx 3.5$ μH each. These circuits are pulsed at this resonance to produce 700 A RMS (∼2 kA peak-to-peak) currents. The switching circuits responsible for power delivery were developed by Eagle Harbor Technologies and are limited to 4 kW operation.

3.2. Inductive probes

The magnetic field measurements presented in this work were acquired using a two-axis Bdot probe constructed according to electric propulsion community best practices [19]. This probe consists of two orthogonally-oriented 1.25 cm diameter by 0.64 cm long fiberglass bobbins, around which 24 AWG enameled copper wire is wound. A pyrex tube is fit over these copper bobbins to protect against damage from the plasma. The two bobbins are offset ∼0.3175 cm from each other both axially and radially.

The 2-axis probe was mounted on a 2-axis motion stage with one of the probe's windings normal to the thruster axis and the other normal to the radial direction. By translating the probe throughout the interior of the thruster and recording the signal at each location, a spatially and temporally resolved map of the induced magnetic field can be measured. Data points were taken at 2 cm intervals both axially and radially inside the cone. 25 thruster pulses were captured at each location for data averaging. We note that variability in the separate shots was low. For example, at the peak value of total integrated current, the standard deviation was approximately 0.75% of the mean.

These probes function according to Faraday's Law, by which a voltage is induced on each wire wrap according to the time rate of change of magnetic flux through the coil. We compute the average magnetic field enclosed by the probe by integrating this signal. In practice, the measured signal has contributions from both the quantity of interest, the driven azimuthal current, and the RMF itself. This poses a measurement difficulty because the latter is often 10–100 times stronger than the former. Therefore because the time scale for changes in the induced azimuthal current is an order of magnitude lower than the fundamental RMF frequency, we reduce the RMF signal by employing a fourth-order RC low-pass filter with a cutoff frequency of 100 kHz. This filtering also eliminates electrostatic coupling which could stem from the ≈10 kV voltage oscillation on the RMF antennas. This coupling would occur at the same frequency as the RMF itself.

The filter and the necessary length of BNC cabling introduced non-ideal circuit effects, requiring a frequency-dependent calibration for these probes to account for both amplitude and phase offset as a function of signal frequency. We followed [20] to accomplish this calibration by generating a transfer function determined by applying a current of known frequency and amplitude into a Helmholtz pair placed over the probe *in-situ*. Figure 3(a) displays a representative signal output for a Bdot probe over the course of a thruster pulse. We note that the signal begins and ends close to zero voltage, consistent with no changing magnetic fields between pulses. The initial

(a)

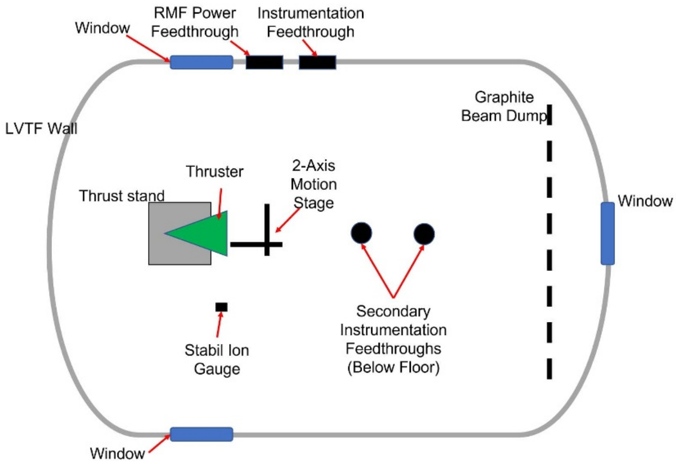

(b)

Figure 2. (a) Photograph of the PEPL RMFv2 on a thrust stand in the Large Vacuum Test Facility at the University of Michigan. (b) Top-down schematic of chamber configuration.

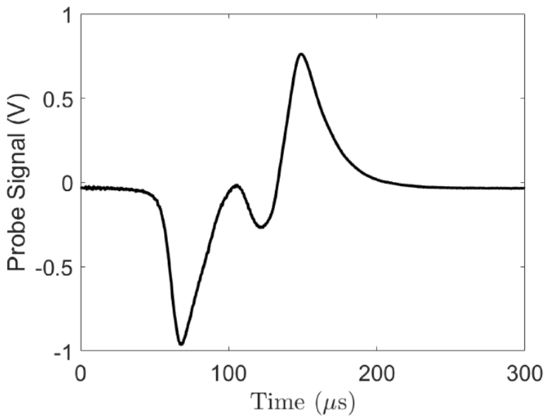

(a)

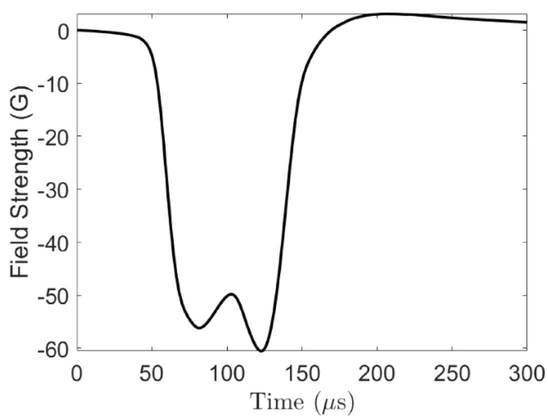

(b)

Figure 3. (a) Uncalibrated Bdot signal trace at the $z = 33$ cm, $r = 0$ cm location, averaged over 100 pulses. (b) Calibrated and integrated signal from (a).

negative swing corresponds to current spinup and plasmoid formation generating magnetic flux in the negative direction, and the positive feature proceeding corresponds to the plasma ejection and relaxation of the plasma current. Additionally, the integral of the initial downward trend appears to be equal to that of the positive swing, a key feature of a correct Bdot probe trace. Despite this, it is common for integration error to become significant when integrating the pulse to generate the actual field measurement as figure 3(b) shows. While this error is relatively small at this location, its relative magnitude can vary across the device and contribute more significantly to uncertainty in total aziumthal current and Lorentz force as we show in greater detail in section 5.

3.3. Test facility

We conducted our tests in the Large Vacuum Test Facility, shown in schematic form in figure 2(b), at the University of Michigan. This is a 6 m wide by 9 m long chamber capable of xenon cryopumping speeds up to 6×10^5 L s^{-1} [21], although we did not utilize the full pumping capacity of the chamber for this campaign. The facility base pressure was $\sim 2\times 10^{-7}$ Torr and operating pressures were $\sim 5\times 10^{-6}$ Torr as measured by a Stabil ion gauge positioned in the plane of the thruster according to electric propulsion community best practices [22]. The thruster was situated approximately 3 meters from a graphite beam dump.

Feedthroughs provided high power connections to conduct current to the RMF antennas as well as device diagnostics. We used Pearson 110 current monitors to measure injected RMF current.

3.4. Operating conditions

The RMF thruster has several operational variables which can be adjusted parametrically to change thruster behavior without any physical reconfiguration. For the measurements presented in this work, we operated the thruster at a steady flow rate of 45 sccm Xe, while the RMF was pulsed at 700 A RMS (2000 A peak-to-peak) for 125 μs pulses at a repetition rate of 155 Hz. This operating point corresponded to the highest total efficiencies from a recent performance study [23]. The pre-pulse neutral density is estimated to be in the $n \approx 1 \times 10^{19}$ range, and at its peak plasma density has been measured at $n_e \approx 1 \times 10^{19}$ 1 m^{-3} with electron temperature peaking at $T_e \approx$ 9 eV [13].

4. Analysis methodology

In this section, we detail the methodology we used to convert the measurements of magnetic field into estimates for current and force density in the thruster. We also describe the procedure for isolating the sources of the measured magnetic fields present in the device.

4.1. Current and force

We calculate the current density in the thruster as a function of time and location using Ampere's Law:

$$\vec{j} = \frac{1}{\mu_0} \vec{\nabla} \times \vec{B} \tag{7}$$

$$j_\theta = \frac{1}{\mu_0} \left(\frac{\partial B_r}{\partial z} - \frac{\partial B_z}{\partial r} \right), \tag{8}$$

where we have made the assumption that the induced plasma current runs only in the azimuthal direction. We assume in equation (7) that displacement currents are negligible in our device per [19]. This stems from the fact that displacement fluctuations are only expected at frequencies greater than the plasma frequency. The characteristic time scale for the RMF is orders of magnitude lower than this frequency (100 GHz). After interpolating the magnetic field measurements inside the thruster cone to allow for smoother derivatives, we calculate the spatially-resolved current density at each time step.

We then compute total current by integrating the current density over the interior of the thruster:

$$I_\theta (t) = \int_A j_\theta \mathrm{d}r \mathrm{d}z. \tag{9}$$

Finally, we arrive at the total force at any given time by volumetrically integrating the Lorentz force:

$$F_z = \int_V B_r j_\theta \mathrm{d}^3 r \tag{10}$$

$$F_r = \int_V B_z j_\theta \mathrm{d}^3 r, \tag{11}$$

where F_r and F_z denote the total Lorentz force on the plasma in the radial and axial directions respectively. Once the force is known, we calculate the impulse per shot by integrating equation (10) with respect to time for the duration of the pulse:

$$I^* = \int F_z \mathrm{d}t, \tag{12}$$

where I^* is the impulse per shot.

4.2. Identifying magnetic field sources

As discussed in section 2, we identify three sources for magnetic field in this thruster: the bias field, which is due to the DC electromagnets surrounding the thruster; the self-field, which is due to the induced plasma currents; and the structure field, which is due to secondary induced currents in conductive structural elements due to the rapid rise of plasma currents.

Differentiating between the bias magnetic field and the other two sources is trivial as the bias field is not detected by the Bdot probes due to its steady nature. To separate the self-field and the structure field, we first calculate the current density in the plasma from the Bdot measurements using equation (2). Because the self-field is directly caused by the plasma current, it can be determined from the current density measurements via Biot-Savart's Law (equation (14) in the appendix). Any magnetic fields not captured by applying Biot-Savart's law to the plasma current must be due to currents outside the plasma. We therefore arrive at the structure field by subtracting the self-field from the measurement:

$$\vec{B}_{\mathrm{struct}} = \vec{B}_{\mathrm{meas}} - \vec{B}_{\mathrm{self}}. \tag{13}$$

Once $\vec{B}_{\mathrm{bias}}$, $\vec{B}_{\mathrm{self}}$, and $\vec{B}_{\mathrm{struct}}$ have been identified, they can each be separately substituted into equations (10) and (11) to determine individual contributions to impulse.

5. Results

In this section, we present the results from our experimental campaign. We first show the RMF current drive for the pulse. We follow this with plots of the magnetic field streamlines produced by overlaying the measured induced magnetic field onto the bias magnetic field. Then we show plots of both current density and total induced current over time, calculated directly from the magnetic field measurements. Finally, we present the thrust values calculated by allowing these currents and magnetic fields to interact via the Lorentz force.

5.1. RMF current waveform

Figure 4(a) displays an image taken from high speed video of the RMF thruster firing. This image was taken at a slightly different thruster configuration than the data presented in section 5, but shows qualitative features of the plume which are conserved between these configurations. In particular, we

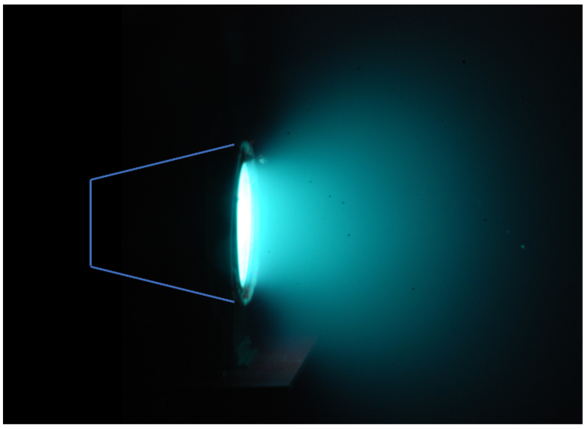

(a)

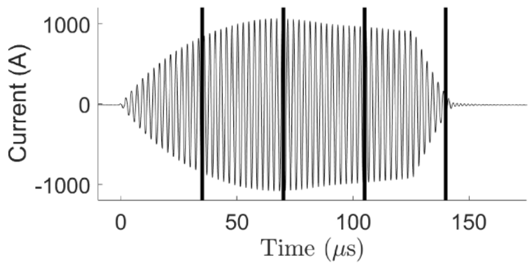

(b)

Figure 4. (a) Long exposure photograph of the RMF thruster 120 μs into a pulse for the 45 sccm Xe, 120 G peak centerline bias field condition. Thruster body outlined in blue. (b) Representative RMF antenna current waveform as a function of time. The vertical bars correspond to time indices for which probe data is presented in this work.

note the sharp contrast in illumination between the expanding plasmoid and the surrounding space which suggests a high density of radiating propellant species, contained by magnetic fields.

Figure 4(b) shows an example of a waveform for the current flowing through the RMF antennas during a representative shot. We observe the current rising over $\sim$60 μs to a maximum value as energy is built up in the resonant circuit. As time progresses, enhanced ionization occurs, allowing for mutual inductance to couple the antennas to the plasma. This changes the effective inductance and resistance of the antenna circuit, reducing the RMF amplitude. This lowered amplitude continues until the pulse ends at the 125 μs point. To provide additional context, we also show on this plot vertical lines which correspond to the time indices that we reference in our following discussion regarding the magnetic fields and currents induced in the thruster.

5.2. Field measurements

Figure 5 shows the magnetic field streamlines and intensity in the thruster at 35 μs intervals. These field lines result from the superposition of the transient induced fields as measured by the two-axis Bdot probe with the steady bias magnetic field. Before approximately 70 μs, no measurable magnetic field is induced. This stems physically from the time required for the RMF current to first reach peak amplitude, then ionize the propellant. At the 70 μs point, the magnetic field is rapidly induced and is strong enough to overcome the bias field near centerline. This results because the direction of RMF rotation was chosen to produce a downstream force when the azimuthal current interacts with the positive radial bias magnetic field. Because the magnitude of the induced field is strong enough to reverse the bias field at centerline but not at the thruster's edge, a separatrix forms. This provides evidence that a field-reversed configuration (FRC) plasmoid has been generated. Peak field strength for the induced magnetic field reaches $\sim$110 G at this 70 μs point. The FRC then translates downstream at a speed of $\sim$2000 m s^{-1} before exiting the cone and dispersing. We estimated this speed by tracking the center of the toroidal field structure where the field magnitude approaches zero.

5.3. Currents

Figure 6 shows the RMF current and the evolution of the current density in the thruster over time, displayed at 35 μs intervals. Similar to the induced magnetic fields shown in figure 5, no current is induced until roughly the 70 μs mark, at which point the current rapidly rises and peaks at a value of $\sim$30 A cm^{-2}. After this time, the distribution in current density spreads axially and propagates downstream. We note that current is primarily driven at larger radial locations, which is consistent with our analysis from equation (2) suggesting that RMF electron entrainment should yield current linearly proportional to radius.

We show the total azimuthal current in figure 7 where we generated these plots by integrating over the current density in the volume following equation (9). For comparison, we also show the envelope of the RMF current extracted from figure 4(b). The uncertainty in the azimuthal current stems primarily from integration error from the Bdot measurement. In keeping with the technique discussed in [19], we estimated this uncertainty by assuming linear growth of integration error up to the maximum value at the end of the pulse.

As can be seen, the induced current peaks at 2.5 kA at the 70 μs mark before decreasing to and remaining at 1.1 kA until the pulse ends at 125 μs. Comparing to the RMF antenna current envelope shown in the same plot, we see that the induced current does not begin to rise until the RMF has ramped in amplitude for 70 μs. We believe this can be attributed to the fact that induced azimuthal current only onsets when the RMF has reached sufficient strength to cause a rapid ionization of the propellant. We note that both the RMF amplitude and induced current trend down after the peak in induced current. For the RMF, we attribute this trend to the presence of plasma altering the effective inductance and resistance of the

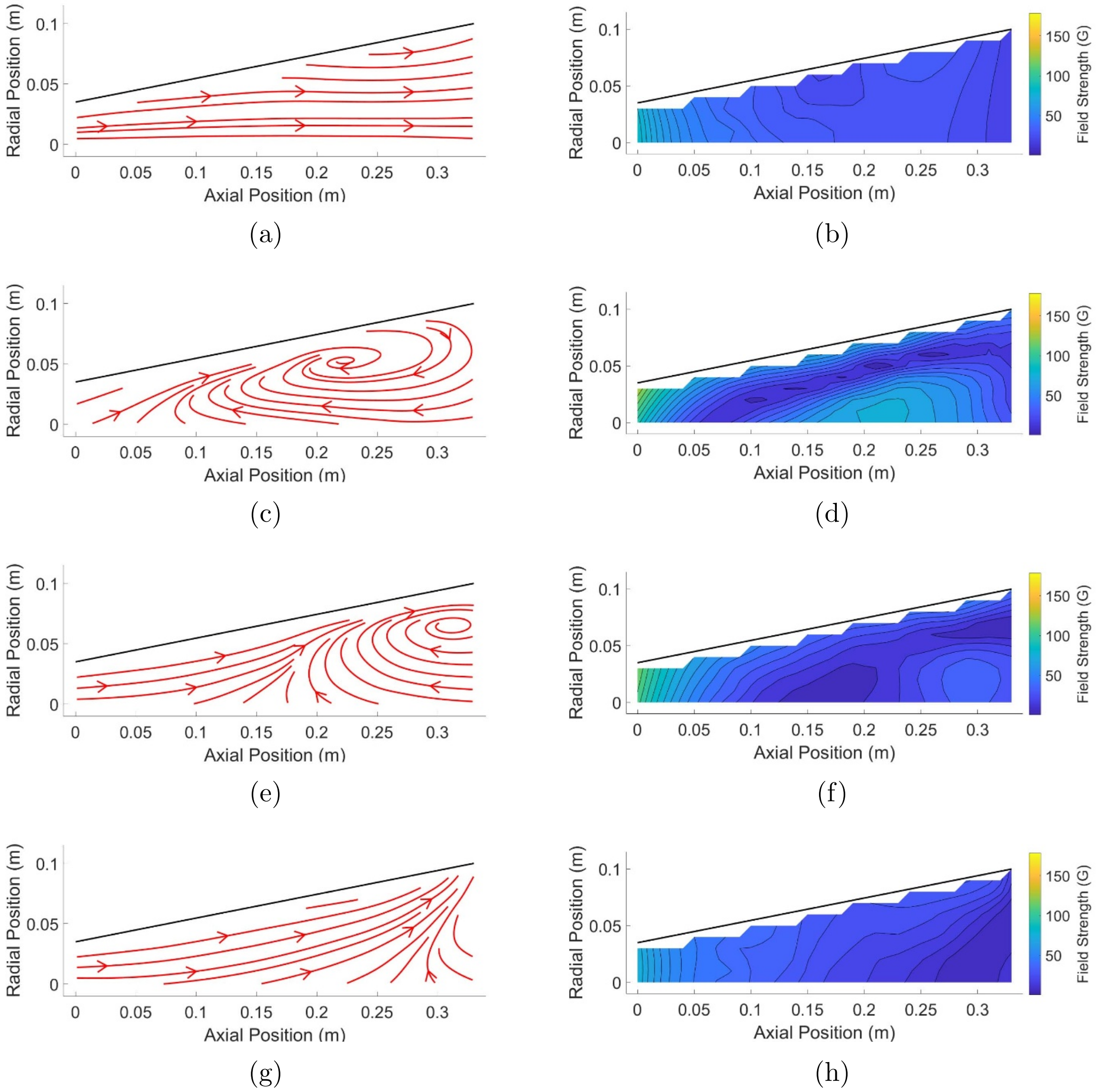

Figure 5. Magnetic field streamlines (left column) and magnitude (right column) at (a), (b) 35 μs, (c), (d) 70 μs, 105 (e), (f) μs, and (g), (h) 140 μs.

antenna (section 5.1). For the azimuthal current, we explain this decrease by the reduction in plasma density in the thruster ([14]). We ascribe this loss of density to a combination of initial plasma ejection and recombination at the thruster walls.

We note here the total current decreases below zero at the end of the shot as well as just before the initial ionization event. We believe these events are caused by measurement error owing to the signal processing, interpolation, and integration involved in producing these plots rather than the existence of actual negative currents.

5.4. Forces

Figures 8(a) and (b) display the forces resulting from the Lorentz interactions in the thruster. We estimate these from equations (10) and (11) where we considered the different sources of magnetic field (self, bias, and structure) and the measured current densities (figure 6). Uncertainty in these plots stems from the integration error in both the current density and magnetic field measurements.

We first consider the individual contributions to force. For the self-field, F_{self}, we see the axial contribution is effectively zero at all times. This agrees with the physical intuition laid out in section 2 that we expect that a system cannot accelerate its own center of mass. On the other hand, conservation of momentum does allow for the nonzero radial component observed. The positive sign indicates a tendency for the plasmoid to expand radially due to this interaction. The temporal profile of the bias force, F_{bias}, follows a qualitatively similar trend as the magnetic fields and currents (figures 5 and 7) in both axial and radial components. This force has near-zero magnitude until roughly 70 μs. At this point, which

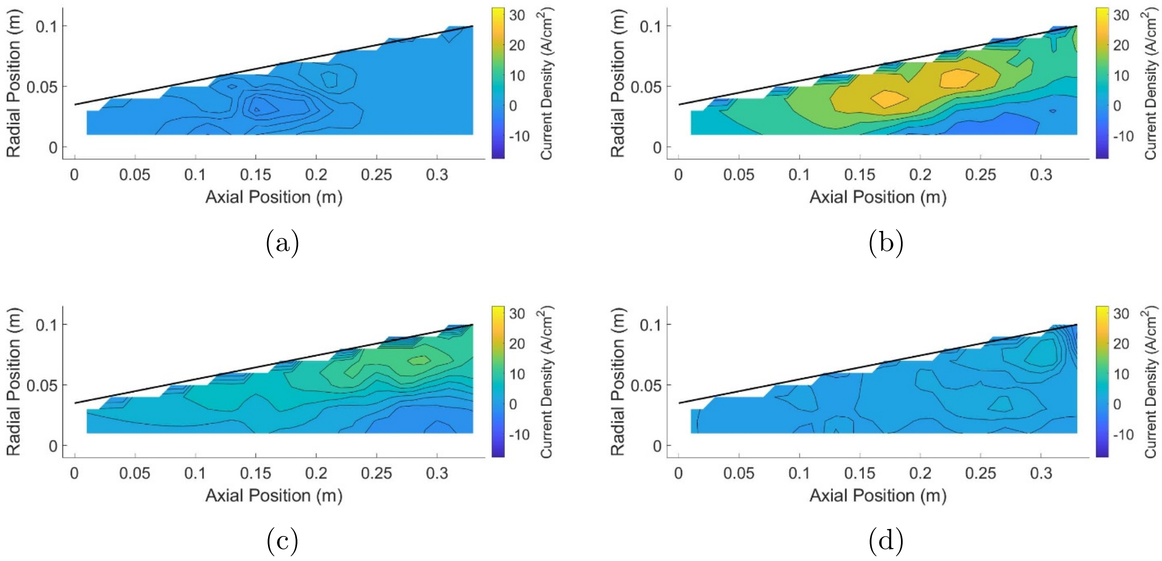

Figure 6. Induced current density in the RMF thruster at (a) 35 μs, (b) 70 μs, (c) 105 μs, (d) 140 μs into the 125 μs pulse.

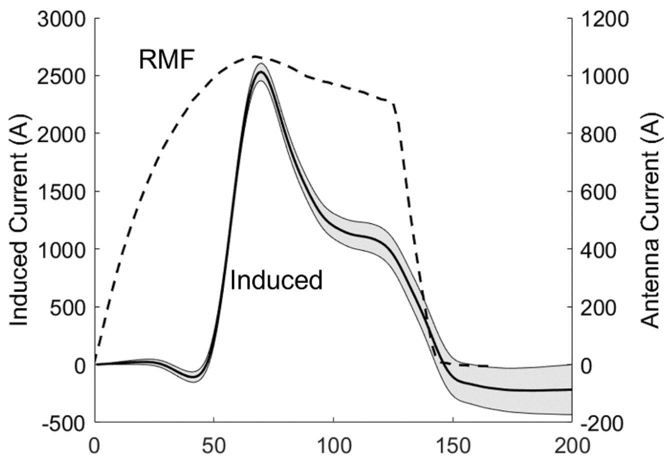

Figure 7. Total induced current in the RMF thruster as a function of time.

is coincident with enhanced ionization, current spin-up occurs, leading to enhanced bias force followed by a plateau until the pulse ends. As can be seen in figure 8(a), the bias force is the primary acceleration mechanism in the first half of the pulse before its magnitude drops below that of the structure force. Meanwhile, figure 8(b) shows that the radial bias field causes the primary radial force throughout the duration of the pulse, providing strong compression.

The structure force, F_{struct}, exhibits its highest axial value after the bias force peaks at $\sim$125 μs when it then dominates the acceleration. We consider two possible explanations for the delay in the axial structure force as compared to the bias force. First, nonzero resistivity in the structural elements could serve to add a time delay to the secondary induced currents and therefore the onset of the structure field. This time delay would be determined by the inductive time constant for each structure. Second, we note that the transient magnetic fields generated by coupled circuit elements are self-repelling. Thus, the force due to the structure field interaction would serve to push the plasma away from any coupled structure. In the case that the plasma current centroid initially forms upstream of a coupled structure, the resulting force would be directed upstream. The structure force subsequently would be balanced or even reversed by the summation of upstream and downstream interactions until the plasmoid could translate sufficiently downstream for the force to become net positive. Indeed, this latter explanation may account for the initial negative structure force exhibited in figure 8(a).

The highest radial value for structure acceleration peaks at $\sim$85 μs. Unlike the axial structure force, the radial component is primarily in the opposite direction of the radial force resulting from the interaction with the bias field. This is unexpected because the currents which induce the structure field should be in the same direction as those responsible for the bias field. This discrepancy may ultimately be a consequence of our limited experimental measurement domain. Because

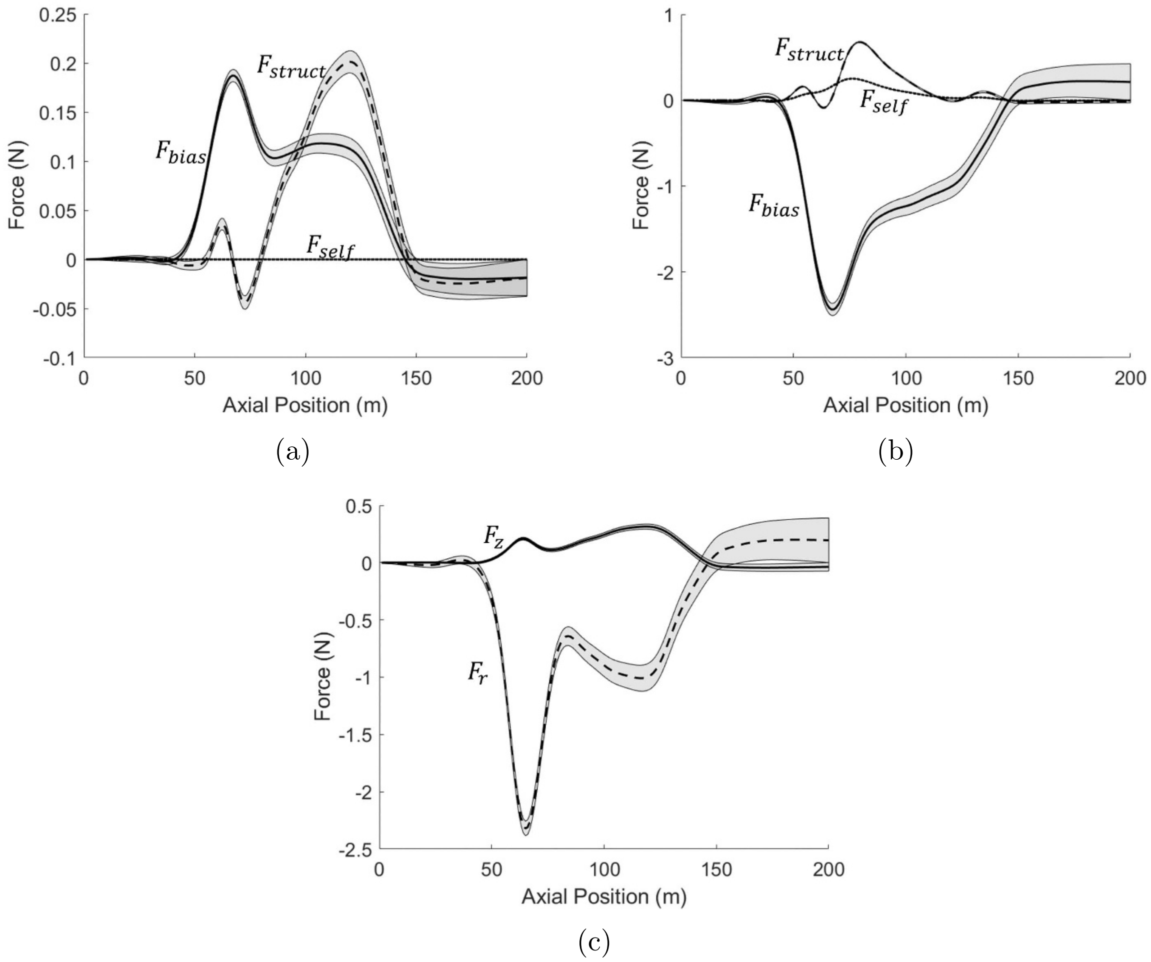

Figure 8. Lorentz force present throughout the RMF pulse broken down to (a) axial contributions by magnetic field source, (b) radial contributions by magnetic field source, and (c) net axial versus net radial force.

the structure field is calculated by subtracting the self field—itself calculated directly from measured plasma current—from the total field measurement, any currents in the plume outside the region of interrogation would be attributed to the structure rather than self field. We ultimately expect that if current measurements further downstream were taken, the radial self force would be greater, and the radial structure force would be primarily negative.

Figure 8(c) shows the total radial and axial contributions to the force on the plasma in the thruster as a function of time. Because the two contributors to axial Lorentz force, the bias and structure forces, peak at different times, the total axial force remains relatively constant throughout the pulse. Meanwhile, the radial inward force is significantly stronger than the total axial thrust force, indicating high levels of compression in the plasma. This type of radial compression is anticipated in any FRC plasmoid and is a hallmark of this plasma structure [5]. Indeed, electron temperature and density measurements taken at the same operating conditions from [14] indicate electron thermal pressure to be of similar order of magnitude to the magnetic pressure. At the 100 μs timestep, for example, peak magnetic pressure, given by $P_{\mathrm{mag}} = \frac{B^2}{2\mu_0}$, reaches $\sim$18 Pa, while thermal pressure at the same time and location is calculated to be $n_e k_B T_e = 12.8$ Pa. We note here that the various contributions to force do not return exactly to zero at the pulse end. This is a non-physical phenomenon which we ascribe to integration error brought about by the discrete nature of our measurements, both temporal and spatial. In reality, these forces will return to zero at pulse-end, and thus we use the discrepancy at the 200 μs point to determine the error owing to this effect.

Finally, we relate these Lorentz force thrust calculations to direct measurement. We calculated the total axial impulse per shot by time-integrating the force. This yielded $16.1 \pm .22\mu$N-s, approximately 42% of which is due to the structure force. Notably, this result underpredicts the 64.3 μN-s measured reported at the same operating conditions from thrust stand measurements. A key implication of this result is that the Lorentz force measured may not fully explain the thrust generation, indicating other acceleration mechanisms may be at play. Indeed, our recent modelling study suggests that a significant portion of thrust may be due to electron pressure at the thruster walls [24].

While electron pressure at the thrust walls approximately explains the difference between calculated Lorentz force thrust and measured thrust, we expect that the estimates of

Lorentz force thrust are likely underpredictions. Because our device–in particular the shape of the bias magnetic field–is qualitatively similar to a magnetic nozzle thruster, the bias field might produce additional thrust owing to the high electron densities ($n_e \geqslant 1 \times 10^{19}$) and temperatures ($T_e \geqslant 8$ eV) measured. However, as the diamagnetic drift and associated Lorentz force which cause magnetic nozzle thrust typically take place further downstream than what is interrogated by our probing techniques in this work [25], we do not expect to resolve these effects.

In summary, in this section we have experimentally characterized in detail the induced currents and magnetic fields in the RMF test article. We have found that the device does in fact lead to FRC formation. Moreover, we have also shown that forces experienced by the plasma are primarily radial, and that the axial forces which do exist are driven by the bias field and the structure field in roughly equal proportion. However, this total force does not fully explain that which we measured via thrust stand, suggesting that non-Lorentz forces may also be key drivers for performance.

6. Discussion

In the following section, we discuss the results from section 5 in the context of the key questions that motivated this study. Specifically, we comment on the efficacy of RMF current drive, the role of Lorentz force in generating thrust, and possible strategies for improving performance.

6.1. Efficacy of RMF current drive

As discussed in section 2, a major benefit from the RMF thruster is its ability to divorce the magnitude of current driven in the plasma from the amplitude of the current in the driving circuit. This contrasts with a more traditional theta-pinch inductive current drive, where large driver current (and therefore voltage) transients are required to drive the internal currents. This poses major challenges to design and robust construction. Our data shows that the RMF current drive as implemented here is successful at producing high plasma currents—driving currents of 2500 A while only requiring RMF current of ~700 A RMS (2000 A peak-to-peak). Leaving aside the poor thrust efficiency measured in this device, it is an encouraging result that the current drive mechanism, which forms the basis of this technology, is effective.

As a direct result of these high levels of driven current, we observed the formation of an FRC plasmoid (figure 5). This was not unexpected given the RMF current drive mechanism was first implemented to drive field reversal for fusion containment applications [5]. From the perspective of thruster performance, the existence of this self-contained structure in principle offers key benefits including increased plasma density [26], reduction in wall losses, and benefits for thrust generation [8]. With this being said, we see the outer separatrix intersects the outer wall of the thruster cone in our thruster configuration, which may ultimately have negated key benefits arising from the FRC's containment. This may have been a chief contributing factor to the high degree of wall losses previously reported for this device [14]. In practice, adjusting the applied field or reducing the driven current may help to pull the separatrix inside the thruster walls, reducing these wall losses.

6.2. Contributions of Lorentz force to RMF plasmoid acceleration

As motivated in section 2, one of the key goals of this study was to assess the degree to which the Lorentz force contributed to thrust in the RMF device. In practice, when comparing the Lorentz force impulse to performance measurements at the same operating conditions, we found that the Lorentz force only accounts for ~25% of the total impulse generated per shot [23]. This is notable because it undermines a conventional understanding of this device as an electromagnetic accelerator.

This invites the question as to what drives most of the acceleration in the thruster. As briefly discussed in section 5, thermal contributions arising from compression of the plasma explain the difference. Inspecting the relative magnitudes of the axial versus radial forces in figure 8(c), it is clear that the majority of the Lorentz forces point inwards in this device, with the inward radial force over five times greater in magnitude than the axial. Given the relative lack of plasmoid radial acceleration over the course of the pulse, as evidenced by figure 5, we can conclude that there is approximate radial pressure balance in the plasmoid. It is possible then that a high electron thermal pressure, driven primarily by high electron densities in the 10^{19} 1 m^{-3} range, is in turn driven by this strong radial compression. This pressure would result in a force equal to $\int_A (nT_{eV} \sin\theta_c)\,\mathrm{d}A$ where A refers to the internal area of the thruster and θ_c is the thruster cone half-angle. Indeed, calculations using electron temperature and density measured with a triple Langmuir probe from [14] suggest that this electron pressure force approximately explains the discrepancy between measured impulse and calculated Lorentz force [24]. We remark here that previous interpretations have also suggested that thermal contributions could be major drivers for thruster operation [8].

In practice, however, we suspect the ideal thrust mechanism for the RMF thruster is the Lorentz force. The thermal force is correlated with high electron temperatures and densities. The high densities carry with them enhanced radiation losses, while both density and temperature increase electron wall losses. A detailed analysis of the scaling of these losses with plasma properties is beyond the scope of this paper—please see [27] for an in-depth discussion. In light of this interpretation, as we discussed in the preceding section in the context of FRC formation, a different bias field that reduces radial force may lead to lower compression, trading thermal heating for improved Lorentz acceleration.

6.3. Strategies for improving performance

One of the major conclusions of our previous work [12] is that performance for the RMF thruster is not competitive compared to state of the art electric propulsion devices. Indeed, efficiencies are over an order of magnitude lower than other inductive devices such as RF magnetic nozzles [15]. Ohmic losses in the RMF antennas and power conditioning circuity, radiation losses, and thermal flux to the walls all have been identified as major loss processes [14]. Section 5 shows that the FRC separatrix intersects the thruster walls, providing a direct thermal short to the thruster boundaries. Moreover, as discussed in the previous section, we have found that thrust generation by Lorentz acceleration is not as dominant as theoretically anticipated.

Given this poor performance, a key question is whether there are paths to improving the performance of RMF thruster. The motivation for this when drawing a contrast to steady-state inductive devices (which already have exhibited higher levels of efficiency than our device) is the potential for improved flexibility in throttling and power density. Leaving aside adjustments to the power conditioning—which may afford marked improvements in performance—our findings about the internal dynamics of the device suggest two possible strategies for improving thruster operation. The first is to amplify the Lorentz acceleration. For the applied field force, we could improve this contribution by adjusting the shape to increase the radial components of the applied field while also increasing magnetic field strength. With that said, while we may be able to optimize geometry by adjusting solenoid position, increasing magnetic field requires more power and stronger magnetics which can be become prohibitive in mass and power.

As a second strategy, we could attempt to enhance the structure field by introducing additional flux conserving elements and optimizing their placement and inductances. This has the additional benefit that the self-field interaction scales quadratically with the RMF driven current, providing nonlinear gains in thrust generation for only moderate adjustments in design and geometry. This would also have the benefit of moving the separatrix radius inward, potentially solving the problem of the separatrix intersecting the thruster walls. FRC compression using flux conservers is a standard practice in the fusion community, and indeed flux conserver conductivity is a key figure of merit in that field [28]. With this being said, we anticipate structure field amplification to be a suboptimal method of increasing performance. Idealized circuit analysis suggests that it could be difficult to fully utilize the inductive energy coupled into the flux conservers as part of this process [29].

7. Conclusions

In this work, we have investigated the current drive mechanism and Lorentz forces present in a RMF thruster via direct inductive probing. We have used the results of a two-axis Bdot probe sweep throughout the thruster interior to calculate induced magnetic fields and current densities. We in turn have related these measurements to effective forces induced on the plasma during RMF operation.

Key amongst our findings is that while the RMF current drive mechanism is successful at generating high levels of azimuthal plasma current and forming a FRC, the magnetic field shape is not effective at leveraging this current to produce thrust. In particular, the Lorentz forces resulting from interactions with the RMF in the axial direction make up less than one third of the total measured force, indicating instead that other factors—likely related to electron pressure—accelerate the flow. This interpretation is consistent with the observation that radial compression induced from the Lorentz acceleration is the largest force in the system, likely giving rise to enhanced electron density and temperature. Notably, however, while thermal acceleration is not inherently undesirable in this device, our results in combination with previously reported studies on our test article indicate that thermally-induced losses to the walls are a major detriment to performance. This can in part be attributed to the fact that the separatrix for our observed FRC actually intersects the thruster walls.

We have discussed these results in the context of strategies for improving thruster performance. For example, we expect that adjustments to the bias magnetic field and thruster shape will be necessary to shift the FRC separatrix inside the thruster walls, which will reduce thermal losses at the walls and shift the thruster toward a Lorentz force dominated mode. Ultimately, because the electron pressure thrust component is so high—which is tied to high thermal losses—the RMF in its present iteration is not an effective thrust generation mechanism. Additional improvement could be achieved by optimizing the placement of flux conserving surfaces around the thruster. In summary, although the RMF performance in this unoptimized test article remains comparatively low, these results ultimately provide new insights for how these devices may be tailored to achieve their full, theoretical potential.

Data availability statement

The data that support the findings of this study are openly available at the following URL/DOI: https://figshare.com/articles/dataset/Magnetic_Field_Data/22303462.

Acknowledgments

We would like to acknowledge NSTRF Grants #80NSSC18K1190 and NSTGRO #80NSSC20K1168 which supported this work. The power supply was developed as part of an SBIR award with Eagle Harbor Technologies, and additional funding was granted by AFOSR Grant FA9550-19-1-0022 from the Space Propulsion and Power portfolio.

Appendix. Thrust scaling

In this section we establish how the three sources of Lorentz force present in the RMF thruster scale with driven plasma current. As the purpose of this discussion is to rigorously demonstrate that these scaling arguments are physically valid rather than to arrive at any numerical result, we leave the equations in the most general vector form possible.

To examine how the Lorentz force scales in an RMF thruster, we seek a functional form for the magnetic field. In the following, we assume cylindrical symmetry in which thruster centerline is aligned with the z-axis and current is only driven azimuthally (see figure 1). We identify three sources of magnetic field. First, the bias magnetic field $\vec{B}_0(\vec{r})$ is generated by the DC currents passing through the bias electromagnets surrounding the thruster. This field is constant with time. Second, the self-field $\vec{B}_{\text{self}}$ results directly from currents in the plasma:

$$\vec{B}_{\text{self}} = \frac{\mu_0}{4\pi}\int_V \frac{j_\theta(\vec{r}')\hat{\theta}\times\vec{r}'}{|\vec{r}-\vec{r'}^3|}\mathrm{d}^3r', \tag{14}$$

where we have employed the Biot-Savart Law, r' is a dummy variable integrated over all space, $\vec{j}$ is the plasma current, and the volume of integration V extends to all of space with nonzero plasma current. We re-write this relation by introducing the variable $\vec{g}(\vec{r},t) = g(\vec{r},t)\hat{\theta}$ which relates the volume integrated magnitude of the induced plasma current I_θ to its distribution: $j_\theta = I_\theta g$. Upon making this substitution, we note that the Biot-Savart Law implies that the magnitude of a magnetic field generated by a current is linearly dependent with the magnitude of the current. This allows us to define some $\vec{\beta}(\vec{r},t)$ such that $\vec{B} = I\vec{\beta}(\vec{r},t)$. Performing both these substitutions, equation (14) yields

$$\vec{B}_{\text{self}} = I_\theta(t)\,\vec{\beta}(\vec{r},t), \tag{15}$$

where

$$\beta_p = \frac{\mu_0}{4\pi}\int_V \frac{\vec{g}(\vec{r},t)\times\vec{r}'}{|\vec{r}-\vec{r'}^3|}\mathrm{d}^3r'. \tag{16}$$

where the subscript p denotes that this β refers to the plasma itself. Physically, this result shows that the magnitude of the plasma's self-field can be related to the product of the magnitude of the driven current and a geometric factor.

As a final contribution to the magnetic field in the plasma, we consider the structure field, $\vec{B}_{\text{struct}}$. This term results from transient currents induced in nearby conductive structural elements by the rapid rise in plasma current when the RMF is pulsed. The bias magnets are an example of a dominant contributor to this effect. To describe this field, we consider that the azimuthal plasma current can be modelled by a collection of discrete, differential current loops, each of which has an area $\mathrm{d}A(\vec{r})$. Therefore, each structural element will have some mutual inductance with each of these differential plasma current loops. Taking the limit of infinitesimally small current elements, the induced EMF or voltage, on the ith structural element is

$$\epsilon_i(t) = \int_A \frac{\mathrm{d}}{\mathrm{d}t}\left(M_i(\vec{r})j_\theta(\vec{r},t)\right)\mathrm{d}A, \tag{17}$$

where M_i is the mutual inductance between the ith structure and the differential current element in the plasma located at $\vec{r}$, and the area of integration A extends to all of space in the r-z plane with nonzero plasma current. Assuming that each structural element has zero resistance, the induced current on the ith structure is

$$\begin{aligned} I_i &= \frac{1}{L_i}\int \epsilon_i(t)\,\mathrm{d}t \\ &= \frac{1}{L_i}\int_A \left(M_i(\vec{r})j_\theta(\vec{r},t)\right)\mathrm{d}A, \\ &= I_\theta\int_A k_i(\vec{r})\sqrt{\frac{L(\vec{r})}{L_i}}\,g(\vec{r},t)\,\mathrm{d}A, \end{aligned} \tag{18}$$

where L_i is the structural element's self inductance and $L(\vec{r})$ is the self inductance is the infinitesimally thin loop of plasma current at location $\vec{r}$. We also have represented the mutual inductance between a plasma current loop and the ith structure loop, as $M_i(\vec{r}){=}k_i(\vec{r})\sqrt{L(\vec{r})L_i}$ where $k_i(\vec{r})$ is a spatially-dependent proportionality constant.

As with the plasma, we can introduce a geometric factor$\vec{\beta}_i(\vec{r})$ which relates the magnitude of the current through structure i to the shape of the magnetic field it produces.

$$\vec{B}_{\text{struct}}(\vec{r},t) = I_\theta\sum_i\left[\vec{\beta}_i(\vec{r},t)\int_A k_i(\vec{r})\sqrt{\frac{L(\vec{r})}{L_i}}\,g(\vec{r},t)\,\mathrm{d}A\right]. \tag{19}$$

Finally, we perform the same $\vec{j} = I\vec{g}$ substitution on equation (4) and substitute the derived values of the various magnetic field components to arrive at the total force

$$\begin{aligned} F = {} & I_\theta\int_V B_{0,r}(\vec{r})\,g(\vec{r},t)\,\mathrm{d}^3r + I_\theta^2\int_V \beta_{p,r}(\vec{r})\,g(\vec{r},t)\,\mathrm{d}^3r \\ & + I_\theta^2\int_V\sum_i\left[\beta_{i,r}(\vec{r},t)\int_A k_i(\vec{r})\sqrt{\frac{L(\vec{r})}{L_i}}\,g(\vec{r},t)\,\mathrm{d}A\right]g(\vec{r},t)\,\mathrm{d}^3r. \end{aligned} \tag{20}$$

ORCID iDs

Christopher L Sercel https://orcid.org/0009-0006-5374-4689
Tate M Gill https://orcid.org/0000-0002-5585-4869
Benjamin A Jorns https://orcid.org/0000-0001-9296-2044

References

[1] Dailey C and Lovberg R 1987 Pulsed inductive thruster component technology *Final Report* (Air Force Astronautics Laboratory)
[2] Hallock A K, Martin A K, Polzin K A, Kimberlin A C and Eskridge R H 2014 Single-and repetitive-pulse conical theta-pinch inductive pulsed plasma thruster performance *IEEE Trans. Plasma Sci.* **43** 433–43
[3] Choueiri E Y and Polzin K A 2006 Faraday acceleration with radio-frequency assisted discharge *J. Propuls. Power* **22** 611–9
[4] National Academies of Sciences Engineering and Medicine 2021 *Space Nuclear Propulsion for Human Mars Exploration* (The National Academies Press) (https://doi.org/10.17226/25977)
[5] Blevin H A and Thonemann P C 1962 Plasma confinement using an alternating magnetic field *Nucl. Fusion Suppl.* **1** 55
[6] Jahn R G 1968 *Physics of Electric Propulsion* (McGraw-Hill)

[7] Slough J, Kirtley D and Weber T 2009 Pulsed plasmoid propulsion: the ELF thruster *31th Int. Electric Propulsion Conf.* pp 20–24
[8] Weber T E 2010 The electrodeless Lorentz force thruster experiment *PhD Dissertation* University of Washington
[9] Kirtley D, Pancotti A, Slough J and Pihl C 2012 Steady operation of an frc thruster on Martian atmosphere and liquid water propellants *48th AIAA/ASME/SAE/ASEE Joint Propulsion Conf. & Exhibit* p 4071
[10] Furukawa T, Takizawa K, Kuwahara D and Shinohara S 2017 Electrodeless plasma acceleration system using rotating magnetic field method *AIP Adv.* **7** 115204
[11] Furukawa T, Takizawa K, Yano K, Kuwahara D and Shinohara S 2018 Spatial measurement in rotating magnetic field plasma acceleration method by using two-dimensional scanning instrument and thrust stand *Rev. Sci. Instrum.* **89** 043505
[12] Sercel C L, Gill T, Woods J M and Jorns B 2021 Performance measurements of a 5 KW-class rotating magnetic field thruster *AIAA Propulsion and Energy 2021 Forum* p 3384
[13] Gill T, Sercel C L, Woods J M and Jorns B A 2022 Experimental characterization of efficiency modes in a rotating magnetic field thruster *AIAA SCITECH 2022 Forum* p 2191
[14] Gill T M, Sercel C L and Jorns B A 2022 Experimental investigation into mechanisms for energy loss in a rotating magnetic field thruster *37th Int. Electric Propulsion Conf.*
[15] Takahashi K 2022 Thirty percent conversion efficiency from radiofrequency power to thrust energy in a magnetic nozzle plasma thruster *Sci. Rep.* **12** 18618
[16] Ahedo E 2009 Cylindrical model of a helicon-generated plasma *31th Int. Electric Propulsion Conf.* (*Ann Arbor, Michigan, USA*) vol 193 (IEPC) p 2009
[17] Furukawa T, Shimura K, Kuwahara D and Shinohara S 2019 Verification of azimuthal current generation employing a rotating magnetic field plasma acceleration method in an open magnetic field configuration *Phys. Plasmas* **26** 033505
[18] Jones I R and Hugrass W N 1981 Steady-state solutions for the penetration of a rotating magnetic field into a plasma column *J. Plasma Phys.* **26** 441–53
[19] Polzin K A, Hill C S, Turchi P J, Burton R L, Messer S, Lovberg R H and Hallock A K 2017 Recommended practice for use of inductive magnetic field probes in electric propulsion testing *J. Propuls. Power* **33** 659–67
[20] Polzin K A 2006 Faraday accelerator with radio-frequency assisted discharge (farad) *PhD Dissertation* Princeton University
[21] Viges E A, Jorns B A, Gallimore A D and Sheehan J 2019 University of michigan's upgraded large vacuum test facility *36th Int. Electric Propulsion Conf.*
[22] Dankanich J W, Walker M, Swiatek M W and Yim J T 2017 Recommended practice for pressure measurement and calculation of effective pumping speed in electric propulsion testing *J. Propuls. Power* **33** 668–80
[23] Sercel C L, Gill T M and Jorns B A 2023 Performance measurements for a 4 KW rotating magnetic field thruster (in preparation)
[24] Sercel C L, Gill T and Jorns B 2023 Performance predictions for CW-mode operation of an rmf thruster *AIAA SCITECH 2023 Forum* p 0449
[25] Takahashi K, Chiba A, Komuro A and Ando A 2016 Experimental identification of an azimuthal current in a magnetic nozzle of a radiofrequency plasma thruster *Plasma Sources Sci. Technol.* **25** 055011
[26] Martin A and Eskridge R 2005 Electrical coupling efficiency of inductive plasma accelerators *J. Phys. D: Appl. Phys.* **38** 4168–79
[27] Gill T M, Sercel C L and Jorns B A 2023 Experimental investigation into efficiency loss in rotating magnetic field thrusters (in preparation)
[28] Myers C, Edwards M, Berlinger B, Brooks A and Cohen S 2012 Passive superconducting flux conservers for rotating magnetic field driven field reversed configurations *Fusion Sci. Technol.* **61** 86–103
[29] Sercel C L, Woods J M, Gill T and Jorns B 2020 Impact of flux conservers on performance of inductively driven pulsed plasmoid thrusters *AIAA Propulsion and Energy 2020 Forum* p 3632